Data Inversion for the Multi-Order Solar Extreme Ultraviolet Spectrograph

J. Lewis Fox[a], Charles C. Kankelborg[a], Thomas R. Metcalf[b]

[a]Montana State University, Department of Physics,
Bozeman, MT 59717, USA
[b]LMSAL, Dept. 79-41, Bldg. 252
3251 Hanover St. Palo Alto, CA 94304, USA

ABSTRACT

The *Multi-Order Solar EUV Spectrograph* (*MOSES*) is a high-resolution, slitless imaging spectrometer that will observe the Sun in the extreme ultraviolet near 304 Å. *MOSES* will fly on a NASA sounding rocket launch in spring 2004. The instrument records spatial and spectral information into images at three spectral orders. To recover the source spectrum an ill-posed inversion must be performed on these data. We will explore two of the techniques by which this may be accomplished: Fourier backprojection and Pixons, constrained by the spatially integrated spectrum of the Sun. Both methods produce good results, including doppler shifts measured to $\frac{1}{3}$-pixel accuracy. The Pixon code better reproduces the line widths.

Keywords: Sun, chromosphere, corona, EUV, imaging, spectroscopy

1. INTRODUCTION

Fast Imaging Spectroscopy (FIS) is a fundamentally powerful observational technique, allowing measurement of two of three pieces of information one can know about the photons coming from a source over a full 2-D field of view. Only the polarization remains unknown in this approach. It is a key technology in understanding the physics of a complicated evolving source, such as the solar atmosphere. The achievement of solar fast imaging spectroscopy has been realized in the realm of visible wavelengths for a number of years, via arrangements of optical narrowband tunable filters (see references for examples).[1,2]

In the Extreme UltraViolet (EUV) FIS has remained elusive, largely due to the difficulty of fabricating optics in this wavelength regime. Imaging spectroscopy in EUV has been achieved by raster scanning a slit across the field of view, as in the case of the *Coronal Diagnostic Spectrometer* (*CDS*) aboard the Solar and Heliospheric Observatory (*SOHO*) spacecraft.[3] Complications arise in the interpretation of the data due to the non-cotemporal nature of the spectra. Indeed, conventional FIS devices can suffer from the same problem for phenomena on time-scales short compared to the time required to build up the image cube.[4] In the case of raster scanning the problem arises from spectra which are not cotemporal with those taken at other spatial locations. In conventional visible light FIS, such as tunable Fabry-Perot filter designs, the problem arises from spectra that are not cotemporal in different parts of the spectrum. The limitation in either case is the scanning speed (either spatial or spectral). A solution is to "make it faster", if that is possible.

By contrast, *MOSES* uses slitless multi-order spectroscopy. In this approach all data are taken simultaneously over the whole field of view. There is no scanning, either spatially or spectrally, and hence no confusion of temporal evolution with spatial or spectral variation. However, *MOSES* must overcome the sparse sampling of information inherent in the instrument. In the following sections we will briefly discuss the instrument (§2) and the inversion problem it presents (§3). We then move on to a description of two of the inversion techniques currently under study, Fourier backprojection (§3.1) and Pixons (§3.2), and the results of trial inversions performed on test data from the *SERTS-95* experiment.[5,6]

Further author information: (Send correspondence to J.L.F)
J.L.F.: Email: fox@mithra.physics.montana.edu, Telephone: 1 406 994 7594
C.C.K.: Email: kankel@solar.physics.montana.edu, Telephone: 1 406 994 7853
T.R.M.: Email: metcalf@lmsal.com, Telephone: 1 650 424 2209

2. INSTRUMENT OPERATING PRINCIPLE

The design of the *MOSES* instrument is covered in more detail in a paper by Kankelborg and Thomas.[7] We will here only summarize the operating principle of the instrument. The interested reader is referred to that paper for more information. Parallel developments in slitless spectroscopy are being pursued by several other research groups in the visible regime.[8–10]

The *MOSES* instrument obtains three images over the field of view, in a narrow passband about the He II 303.8 Å emission line. These three images correspond to spectral orders $n = -1, 0, +1$. The grating has dispersion only in one direction, defined as the x axis. Since there is no slit, each image is an overlapping series of images from the spectral lines in the passband, in the case of *MOSES* only two: He II λ303.8 and Si XI λ303.3. Each slice along the y axis will be independent of the others. To simplify the analysis conceptually and in practice we consider a fixed value of $y = y_0$ and think of the data as 3 1-D intensity images. The Sun is an image "cube", a 2-D image which is a function of (x, λ). The data are functions of a single coordinate $(x + n\lambda)$, where x and λ are in pixel units. The mapping relating $I(x, \lambda)$ to $I_n(x + n\lambda)$ is identically analogous to tomography of a hybrid "object" in spatio-spectral coordinates along three directions at $(-45°, 0°, 45°)$ (figure 1). Analysis of the data can be carried out by forward-modeling or inversion to recover the image "cube" representing the part of the Sun which fits in our field of view and passband. This paper discusses inversion by two distinct methods, *fourier backprojection* and *Pixon reconstruction*.

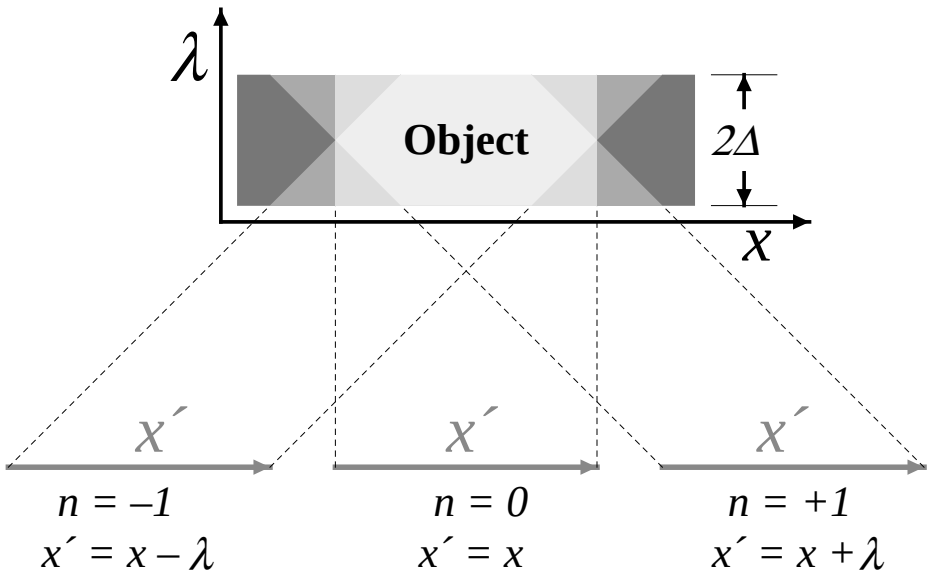

Figure 1. A multi-order slitless spectrograph is equivalent to tomography of an object in (x, λ) space from several different "viewing angles".

3. INVERSION OF *MOSES* DATA

Inverting the data functions I_n to recover the image cube I is clearly an ill-posed problem. The data functions represent $3N$ pieces of information while the cube contains (approximately) NM, where N and M are the number of x and λ pixels respectively. As a result there are an infinite number of cubes which can accomodate the data. Compounding this problem, the data functions do not sample precisely the same sections of the cube. As figure 1 shows, some sections are sampled by only 1 or 2 lines of sight.

We deal with these issues by taking advantage of prior information and careful instrument design choices. As shown by Kankelborg and Thomas,[7] the *MOSES* nullspace is filled by things which contain negative intensity. The instrument passband has been chosen to be narrow enough that only two spectral lines are contained therein.

Because the passband is sparse many potential cubes contain nullspace elements with negative intensities in places where there are very few photons. These can be eliminated by positivity constraints. To deal with the effects of sampling at the edges, we only attempt to reconstruct the part of the cube sampled by two or more orders. The design of the instrument further diminishes the effect of this ambiguity by making the x direction much longer than the λ direction ($N \gg M$). *MOSES* has $N = 2048$ x-pixels but only $M \sim 64$ λ-pixels.

We also have a great deal of information about the spectral lines in our passband. Prior experiments have shown that these lines have Gaussian profiles,[11] established their average integrated linewidths, and measured the separation of the line centers.[5] With simulated *MOSES* data, we have found it possible to locate the line center by cross-correlation of the three observed orders. For the present numerical simulations, we implement this complex prior knowledge by assuming that we know the integrated spectrum or "infinite" order projection (the line-of-sight looking into the cube from the side, at 90°). For the purposes of this study we have used the *actual* ∞ order from our *SERTS-95* test data. The ∞ order data are noised just like the "observed" data before passing to the inversion procedure. We plan to investigate systematically the sensitivity of the inversion to the ∞ order in a future study.

Other common heuristics, such as local smoothness and Maximum Entropy, are available but have not been used explicitly (some of them are inherent in the Pixon method, see §3.2). We can also construct heuristic functions encapsulating the physics of line formation if we wish.[12] In the present implementation we have chosen not to add this layer of complexity.

3.1. Fourier Backprojection

The Fourier backprojection method treats the inversion as a traditional tomography problem. All measurements during the inversion are in pixel units and there is no indication at any point that one axis is a λ axis rather than a y axis. The reconstruction makes use of the Fourier Slice Theorem[13] and a positivity constraint.

By the Fourier Slice Theorem, the Fourier transforms of the data functions are slices of the Fourier transform of the cube (see figure 2). The data are transformed and placed in their slices in a blank Fourier transform (the ∞ order is padded with zeros to make the transform square). This is inverse transformed back to real space. Because the Fourier transform was undersampled this results in many negative pixels in the resulting image. Negative pixels are zeroed in coordinate space and the non-negative image is tranformed back into Fourier space. The new transform has non-zero elements in the wedges (see figure 2) that previously were not populated by data. It also has altered values for the data functions. These slices are reloaded with the correct (measured) values. We now transform back to real space and iterate this procedure until the resulting image in real space has negligible negative intensity (negligible is defined by the convergence criterion $\sum(I < 0) \leq \sqrt{\sum I}$).

Figures 3 and 4 show the results of a trial inversion performed with the backprojection method. The algorithm assures that the fit to the data is essentially perfect ($\chi^2 \sim 0$). The plot in figure 4 shows the 1st, 2nd, and 3rd quartiles of the He II line profile. The differences (mean and RMS) between the true and reconstructed data are summarized in table 4.

3.2. Pixon Inversion

Pixon reconstruction is a powerful Bayesian technique for restoring or reconstructing complexly encoded image data. The basic ideas behind the technique and its use are covered in a variety of references.[14–19] The technique relies on ideas from information theory. The image model with minimal information content is best. One tries to specify the image using the smallest possible number of parameters. In the Pixon approach one allows the image model to change during the reconstruction while attempting to minimize both the goodness-of-fit (GOF) and the information content of the image (quantified as the number of Pixons). In this regard the Pixon prior is very similar to Maximum Entropy.

One common image model, which we use for *MOSES* reconstructions, is a pseudoimage/Pixon-map pair with fuzzy Pixons. In practice one specifies a set of Pixons with which to model the image. This set is not the optimal set of Pixons for a generic image; it's selection is driven by the kind of image one expects to find. The reconstruction only approaches the ideal of minimal information content as a result of the limited selection of Pixons in the basis set. The image is a "convolution" of the pseudoimage with the Pixon map, $\mathbf{I} = \mathbf{M} \otimes \mathbf{P}$. The

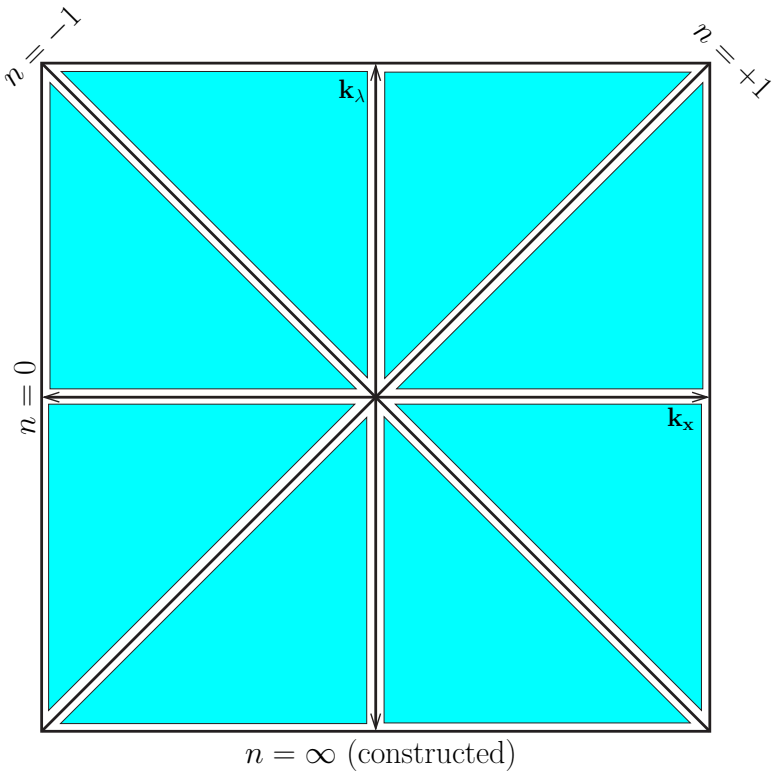

Figure 2. The Fourier space representation of a spectral cube. The dark lines are measured by *MOSES* or constructed from prior knowledge. The shaded wedges are constrained by the requirement of non-negativity in real space.

"$\otimes$" operator is not a true convolution, but very similar. The Pixon map specifies the fuzzy Pixon basis function to use at a given pseudoimage position. The fuzzy Pixons are normalized shape functions (convolution kernels) which give the size scale and shape of the information content in the image at that place. The pseudoimage intensity at each point is multiplied by the appropriate shape function, which spreads this intensity out over some area. Both the pseudoimage and Pixon map are allowed to vary in order to accomplish the twin goals of minimizing information and maximizing fidelity to the measured data functions. The pseudoimage is easily chosen to be strictly non-negative, as are the Pixon basis functions. The convolution process which generates the image from the pseudoimage and the Pixon map enforces both smoothness and positivity.

We have performed a reconstruction with this Pixon method. The initial Pixon map is chosen to consist entirely of the largest size Pixon. The pseudoimage is initialized with two lines at approximately the locations of the He II and Si XI line. The pseudoimage and Pixon map are optimized independently of each other to reduce the GOF (we have chosen χ^2) criterion. When the GOF has been minimized over $\mathbf{P}$ with $\mathbf{M}$ held constant we allow the next smallest Pixon shape function to be put into the map and then minimize χ^2 over $\mathbf{M}$ with $\mathbf{P}$ held constant. At the end of this optimization we return to minimizing over $\mathbf{P}$ with $\mathbf{M}$ constant. At the end of each such iteration we reset the entire Pixon map to the largest size and allow one smaller size from the Pixon basis than was allowed in the last iteration. The procedure terminates on the $\mathbf{P}$ optimization after the last Pixon in the basis has been added to the available Pixons.

Our Pixon basis for this reconstruction is shown in figure 5. The Pixons are elliptical truncated Gaussians with major axis aligned with the λ direction. The shape function is defined by

$$S(x,\lambda) = \frac{R(x,\lambda)}{\int R(x,\lambda) dx d\lambda}$$

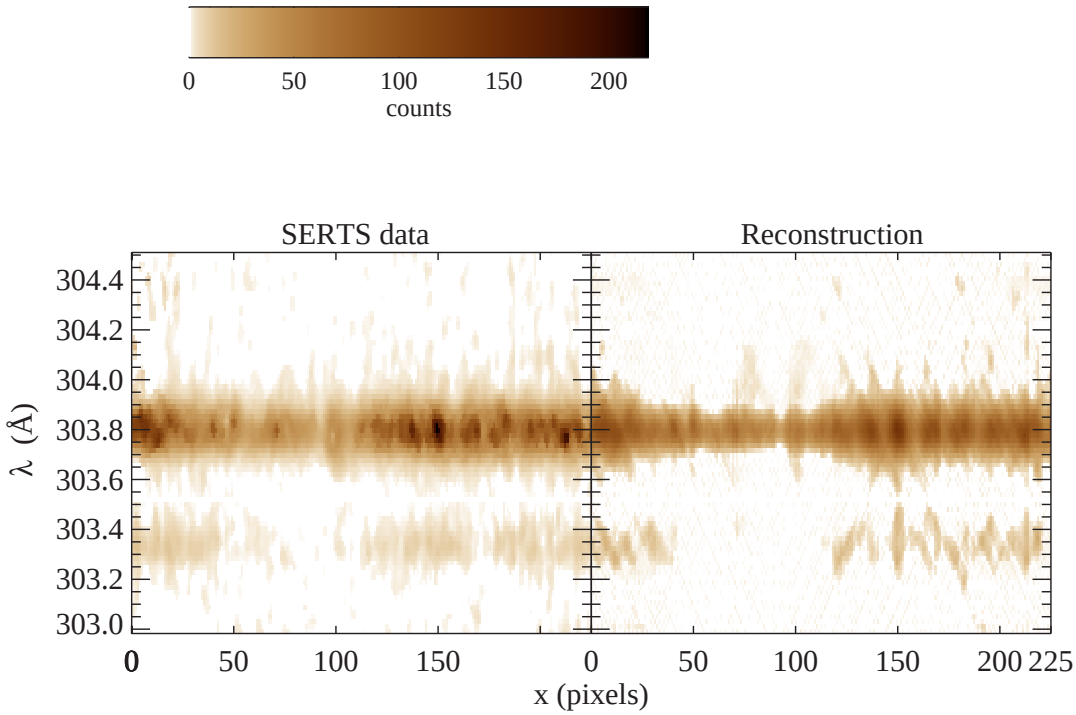

Figure 3. Original *SERTS-95* data vs. the Fourier backprojection reconstruction. The *SERTS-95* data have been rescaled to correspond to anticipated *MOSES* count rates.

where

$$R(x,\lambda) = \exp\left(-\frac{(x-c_x)^2}{2r_s^2} - \frac{(\lambda-c_\lambda)^2}{2(r_s+3)^2}\right)$$

The constants (c_x, c_λ) and r_s define the center and minor axis scale of each Pixon. The Pixons all have a common center. The largest Pixon in figure 5 is circular rather than elliptical. This Pixon is intended to cover large areas of nearly uniform intensity. These will usually be nearly zero intensity regions for solar images in this passband and don't necessarily have any particular shape. The other Pixons are intended to cover the spectral lines, which are believed to be gaussian in the wavelength axis.

This Pixon basis is far from optimal. There are not enough Pixons in it and no Pixons which are longer in the x direction. Such Pixons might be thought appropriate for fitting sections of spectral lines where the width is nearly constant. Furthermore this basis is incomplete, in that it cannot produce a generic image because it contains no Pixon which is the size of one pixel. These problems with the basis are evident in the comparison of the data with the reconstruction which is presented in figure 6. The reduced χ^2 for each of the orders $(+, -, 0, \infty)$ are $(1.07, 1.05, 1.25, 4.54)$. Clearly the χ^2 is not yet optimal. The quartiles plot for the central 225 pixels (equivalent to the plot for the Fourier backprojection method) is presented in figure 7. Table 4 summarizes the success of both Fourier backprojection and Pixons in reconstructing line profile parameters.

4. DISCUSSION

We have presented two methods for reconstructing an image cube from *MOSES* data. Our Pixon implementation is still very new and incomplete. Although work on the Fourier backprojection method has not ceased, it is far

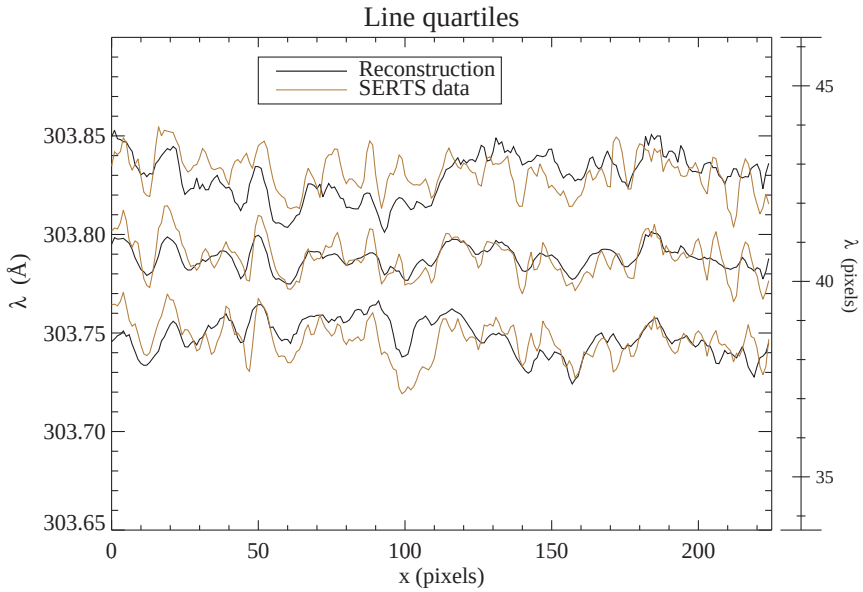

Figure 4. 1st, 2nd, and 3rd quartiles of the *SERTS-95* image and the Fourier backprojection reconstruction.

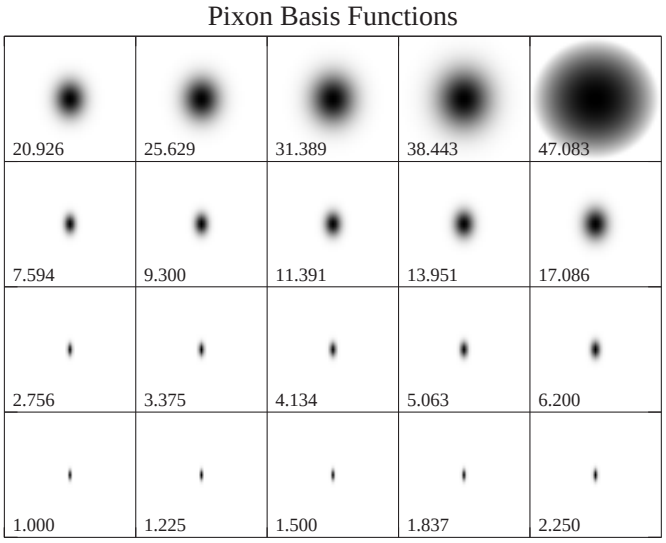

Figure 5. The Pixon basis for this reconstruction. The effective minor axis size is given in the lower left corner of each box. The major axis is 3 pixels larger than this value. The largest Pixon is circular rather than elliptical.

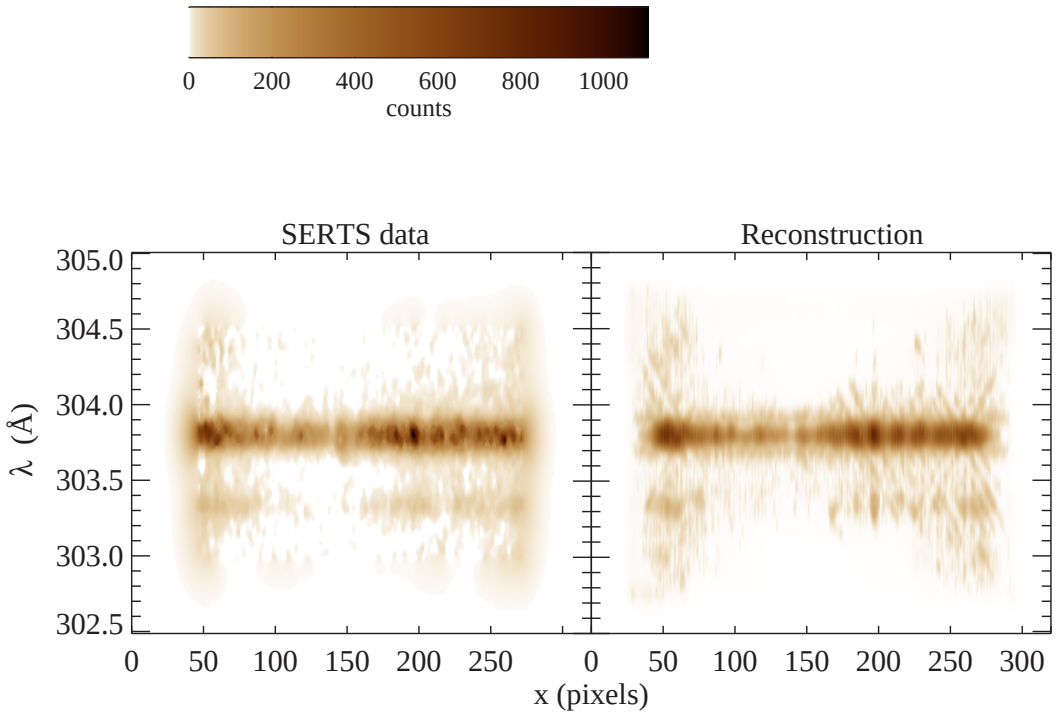

Figure 6. A comparison of *SERTS-95* data (rescaled) with the reconstruction via the Pixon method. The *SERTS-95* data has been extended so that it goes to zero smoothly in all directions at the edges.

closer to maturity than the Pixon method.

The methods have different computational and theoretical characteristics. The Fourier method is fast and provides a "quick-look" data product with roughly the right character. The Pixon method is based on a technique that has proven powerful and robust in other applications.[17–19] We believe Pixons may yield the best reconstructions possible. This method is slow and may require tuning for the *MOSES* application, especially in the choice of Pixon basis.

Cursory inspection of figures 3 and 6 leads to the conclusion that these two methods produce comparable reconstructions. The quartile plots in particular give us confidence that both methods are generally able to reproduce the features of the strong He II line. The general similarity between these two methods should be taken as validation that the *MOSES* concept is sound. However, there are detectable differences between the two reconstructions. To be quantitative we take the quartiles as measures of the line parameters of physical interest, line center and width. These would allow us to produce, for instance, dopplergrams in He II and temperature maps. The errors in line center and line width (based on quartiles) from each inversion method are summarized in Table 4. Both methods centroid the line profile to $\sim \frac{1}{3}$ pixel, which corresponds to approximately 7 mÅ or 7 km/s velocity discrimination. The Fourier backprojection infers a linewidth that is systematically narrow. The Pixon method yields superior, sub-pixel line width determination.

It is apparent from the reconstructed images (figures 3 and 6) recovers the relatively weak Si XI line accurately. Perhaps a fully matured Pixon method will allow recovery of Si XI intensity. This would undoubtedly also lead to improved determination of the He II line profile, which is likely limited by noise from the unrecovered Si XI.

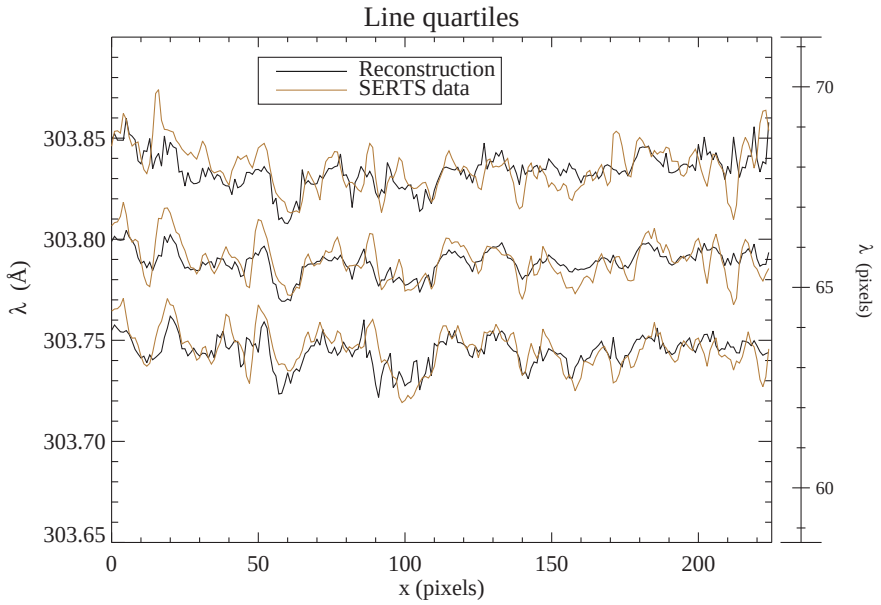

Figure 7. Quartiles plot for the Pixon reconstruction similar to figure 4.

Table 1. Differences between true and reconstructed line profile parameters. Line center and linewidth errors are in pixels. For each parameter, a mean offset and RMS error are given. One *MOSES* pixel is approximately 20 mÅ.

	center (median)		width (quartiles 1-3)	
Algorithm	mean	RMS	mean	RMS
Fourier	-0.01	0.32	-0.19	0.97
Pixon	-0.04	0.36	-0.04	0.59

In summary, our early investigations into the inversion of *MOSES* data are promising. It appears that we will be able to use *MOSES* to make meaningful measurements of velocities in the transition region with resolution less than 10 km/s. Such measurements will have implications for our understanding of the mechanism producing the anomalously large He II intensity in the transition region and the proposed "velocity redistribution" model, which may explain the discrepancy between data and theories of radiative transfer in the chromosphere and transition region.[11] It remains to be seen whether we will be able to make usable measurements of the Si XI line. We also hope for improvements in our ability to measure line widths as we refine our reconstruction methods.

5. ACKNOWLEDGEMENTS

This work has been supported by NASA grant NAG5-10997 and NASA GSRP fellowship NGT5-50471. JLF gratefully acknowledges the helpful comments and suggestions of Dr Curt Vogel during his course on Inversion Problems in Image Processing and Adaptive Optics at MSU, Fall 2002.

REFERENCES

1. P. H. Scherrer, R. S. Bogart, R. I. Bush, J. T. Hoeksema, A. G. Kosovichev, J. Schou, W. Rosenberg, L. Springer, T. D. Tarbell, A. Title, C. J. Wolfson, I. Zayer, and MDI Engineering Team, "The Solar Oscillations Investigation - Michelson Doppler Imager," *Sol. Phys.* **162**, pp. 129–188, 1995.

2. C. Bendlin, R. Volkmer, and F. Kneer, "A new instrument for high resolution, two-dimensional solar spectroscopy," *A&A* **257**, pp. 817–823, Apr. 1992.
3. B. J. Kent, R. A. Harrison, E. C. Sawyer, R. W. Hayes, A. G. Richards, J. L. Culhane, K. Norman, A. A. Breeveld, P. D. Thomas, A. I. Poland, R. J. Thomas, W. T. Thompson, B. R. Aschenbach, H. W. Braeuninger, O. Kjeldseth-Moe, M. Kuehne, J. Hollandt, W. Paustian, and B. J. Bromage, "Coronal Diagnostic Spectrometer: an extreme-ultraviolet spectrometer for the Solar and Heliospheric Observatory," in *Proc. SPIE Vol. 2517, p. 12-28, X-Ray and EUV/FUV Spectroscopy and Polarimetry, Silvano Fineschi; Ed.*, **2517**, pp. 12–28, Oct. 1995.
4. A. Settele, T. A. Carroll, I. Nickelt, and A. A. Norton, "Systematic errors in measuring solar magnetic fields with a FPI spectrometer and MDI," *A&A* **386**, pp. 1123–1128, May 2002.
5. J. W. Brosius, J. M. Davila, and R. J. Thomas, "Solar Active Region and Quiet-Sun Extreme-Ultraviolet Spectra from SERTS-95," *ApJS* **119**, pp. 255–276, Dec. 1998.
6. J. W. Brosius, R. J. Thomas, and J. M. Davila, "SERTS-95 Measurements of Wavelength Shifts in Coronal Emission Lines Across a Solar Active Region," *ApJ* **526**, pp. 494–504, Nov. 1999.
7. C. C. Kankelborg and R. J. Thomas, "Simultaneous imaging and spectroscopy of the solar atmosphere: advantages and challenges of a 3-order slitless spectrograph," in *Proc. SPIE Vol. 4498, p. 16-26, UV/EUV and Visible Space Instrumentation for Astronomy and Solar Physics, Oswald H. Siegmund; Silvano Fineschi; Mark A. Gummin; Eds.*, pp. 16–26, Dec. 2001.
8. M. R. Descour, C. E. Volin, E. L. Dereniak, T. M. Gleeson, M. F. Hopkins, D. W. Wilson, and P. D. Maker, "Demonstration of a computed-tomography imaging spectrometer using a computer-generated hologram disperser," *Appl. Opt.* **36**, pp. 3694–3698, June 1997.
9. D. W. Wilson, P. D. Maker, and R. E. Muller, "Reconstructions of computed-tomography imaging spectrometer image cubes using calculated system matrices," in *Proc. SPIE Vol. 3118, p. 184-193, Imaging Spectrometry III, Michael R. Descour; Sylvia S. Shen; Eds.*, pp. 184–193, Oct. 1997.
10. C. E. DeForest, "Stereoscopic Spectroscopy: A New Technique for Rapid Magnetography," in *Proc. of the 3rd Solar Workshop on Spectropolarimetry, Trujillo-Bueno, J.; Sanchez-Almeida, J.; Eds., ASP Conf. Ser. 307 (in press)*, 2003.
11. V. Andretta, S. D. Jordan, J. W. Brosius, J. M. Davila, R. J. Thomas, W. E. Behring, W. T. Thompson, and A. Garcia, "The Role of Velocity Redistribution in Enhancing the Intensity of the HE II 304 Å Line in the Quiet-Sun Spectrum," *ApJ* **535**, pp. 438–453, May 2000.
12. J. L. Fox and C. C. Kankelborg, "A Parametric Inversion Technique for MOSES Data," *American Astronomical Society Meeting* **200**, pp. 0–+, May 2002.
13. A. C. Kak and M. Slaney, *Principles of Computerized Tomographic Imaging*, IEEE Press, New York, 1988.
14. R. C. Puetter, "Pixons and Bayesian image reconstruction," in *Proc. SPIE Vol. 2302, p. 112-131, Image Reconstruction and Restoration, Timothy J. Schulz; Donald L. Snyder; Eds.*, pp. 112–131, Sept. 1994.
15. R. C. Puetter, "Information, language, and pixon-based image reconstruction," in *Proc. SPIE Vol. 2827, p. 12-31, Digital Image Recovery and Synthesis III, Paul S. Idell; Timothy J. Schulz; Eds.*, pp. 12–31, Oct. 1996.
16. R. K. Piña and R. C. Puetter, "Bayesian image reconstruction - the pixon and optimal image modeling," *PASP* **105**, pp. 630–637, June 1993.
17. D. D. Dixon, W. N. Johnson, J. D. Kurfess, R. K. Pina, R. C. Puetter, W. R. Purcell, T. O. Tuemer, W. A. Wheaton, and A. D. Zych, "Pixon-based deconvolution.," *A&AS* **120**, pp. C683+, Dec. 1996.
18. D. Alexander and T. R. Metcalf, "A Spectral Analysis of the Masuda Flare Using YOHKOH Hard X-Ray Telescope Pixon Reconstruction," *ApJ* **489**, pp. 442–+, Nov. 1997.
19. T. R. Metcalf, H. S. Hudson, T. Kosugi, R. C. Puetter, and R. K. Pina, "Pixon-based Multiresolution Image Reconstruction for Yohkoh's Hard X-Ray Telescope," *ApJ* **466**, pp. 585–+, July 1996.